



Research articles

Spin-orbit torque induced multi-state magnetization switching in Co/Pt hall cross structures at elevated temperatures

G.J. Lim, W.L. Gan, W.C. Law, C. Murapaka, W.S. Lew*

School of Physical and Mathematical Sciences, Nanyang Technological University, 21 Nanyang Link, Singapore 637371, Singapore

A B S T R A C T

We demonstrate spin-orbit torque (SOT) driven multi-state magnetization switching in Co/Pt Hall crosses in the presence of varying externally applied in-plane (IP) bias fields from room temperature (RT = 295 K) to 360 K. *In-situ* Kerr imaging at various resistance states reveal the evolution of up and down magnetic domain expansion due to current-induced SOT switching. The control of magnetization states in the Hall cross is attributed to the inhomogeneous current-density and current-induced effective out-of-plane field due to the device geometry. The critical switching current density scales inversely with device temperature, and the SOT-driven change in Hall resistance varies across device temperatures and IP fields. Subsequently, the current-induced SOT efficiency, χ_{sat} , and the Dzyaloshinskii-Moriya interaction effective field, H_{DMI} , at RT and 360 K are determined using the chiral domain wall model and current-induced loop-shift method. The χ_{sat} and H_{DMI} values are found to decrease by $\sim 26\%$ and $\sim 15\%$, respectively, with increasing device temperature. These results demonstrate the thermal sensitivity of current-induced SOT magnetization switching in multi-state devices.

1. Introduction

Generation of spin current for spin-orbit torque (SOT) driven magnetization switching in heavy metal (HM)/ferromagnet (FM) heterostructures has attracted a lot of attention recently for fundamental understanding as well as for device applications. One advantage of SOT is the elimination of an additional ferromagnetic layer for spin polarization of conduction electrons as required in the conventional spin-transfer torque effect. The SOT originates from strong spin-orbit coupling (SOC) via the spin Hall effect (SHE) [1,2], and/or the Rashba effect [3–9] in HMs. The effects of SOT on local magnetization in a FM is dependent on structural inversion asymmetry (SIA), and can be achieved by sandwiching the FM between layers of dissimilar materials or thicknesses. Since its discovery, SOT has been of great interest in applications that rely on fast domain wall propagation [10–12], efficient magnetization switching [2,9,13], as well as for sustaining steady state excitation in ferromagnetic nanostructures [14,15].

More recently, Kurenkov *et al.*, have reported current-driven SOT analogue switching behaviour characterised by the intermediate resistance states which was observed for device dimensions larger than the magnetic domain size [16]. Such SOT devices are promising in applications of neuromorphic engineering due to their non-volatile analogue behaviour [17–21]. However, CMOS-integrated spintronic devices will be subjected to thermal effects due to thermal dissipation from electronic transistor operations. While binary MTJs can afford large read and write margins [22,23], the impact of elevated operating

temperature on SOT-driven devices with multi-state behaviour remains unexplored.

In this work, we demonstrate multi-state characteristics in a Co/Pt multilayer Hall cross device. The intermediate resistance states due to the formation of magnetic domains across the device are captured by *in-situ* Kerr microscopy. The multi-state behaviour is shown to be attributed to an inhomogeneous current density profile across the device junction. The effects of current-induced SOT magnetization switching from room temperature (RT = 295 K) to 360 K on the change in Hall resistance ΔR_H across varying in-plane (IP) bias fields H_x are summarised in switching phase diagrams.

A thin film stack of Ta (5)/Pt (3)/[Co (0.6)/Pt (0.6)]₄/Co (0.6)/Ta (5) was deposited on high resistivity Si/SiO₂ substrates by magnetron sputtering. The numbers in parentheses indicate the nominal thickness of each layer in nm. Vibrating sample magnetometry measurements of the blanket films at room temperature indicate perpendicular magnetic anisotropy with a coercivity $H_c \approx 300$ Oe as shown in Fig. 1a. The effective anisotropy field is determined from the hard axis hysteresis measurement to be $H_{k,eff} \approx 10$ kOe. The Co/Pt multilayer shows strong as-deposited perpendicular magnetic anisotropy without the need for annealing. The film is subsequently patterned into a Hall cross structure comprising $5 \mu\text{m} \times 50 \mu\text{m}$ bars using electron beam lithography and Ar ion milling techniques. Ti (5)/Cu (100)/Ta (5) electrodes serve as electrical contacts to inject the pulse write and DC probing current as well as for Hall voltage measurements. Fig. 1b shows the schematic diagram of a patterned device with the electrical contacts for the pulse

* Corresponding author.

E-mail address: wensiang@ntu.edu.sg (W.S. Lew).<https://doi.org/10.1016/j.jmmm.2020.167201>

Received 11 May 2020; Received in revised form 21 June 2020; Accepted 28 June 2020

Available online 03 July 2020

0304-8853/ © 2020 Elsevier B.V. All rights reserved.

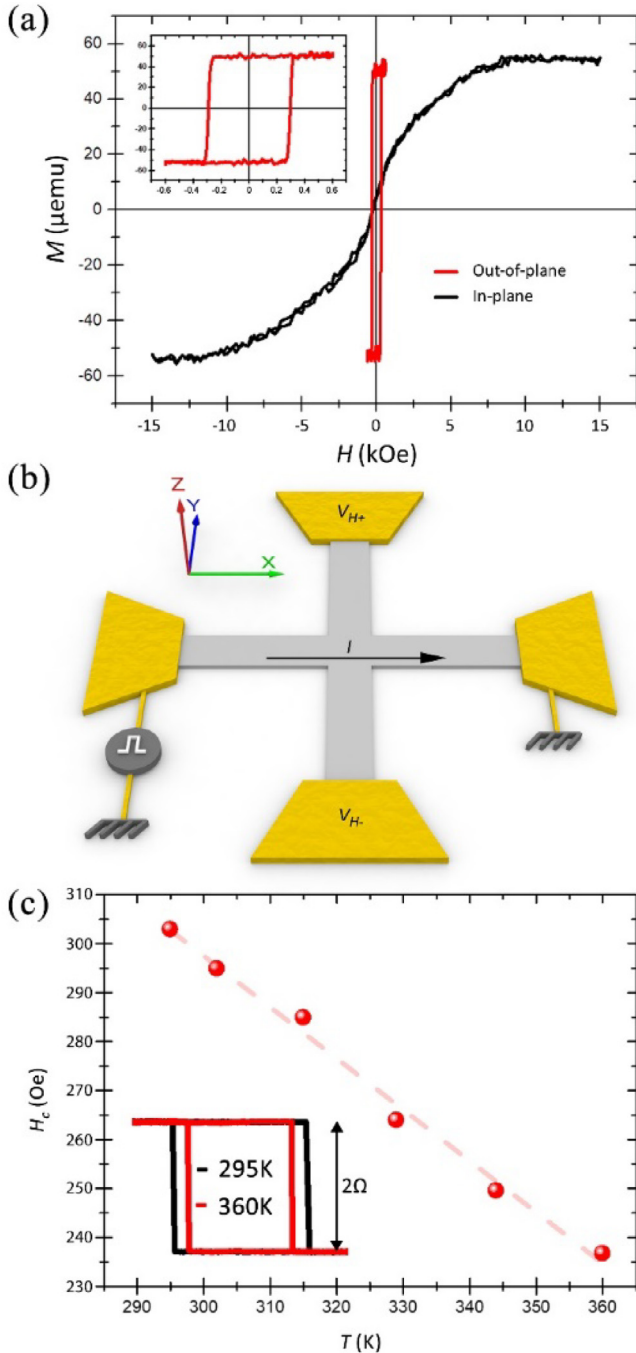


Fig. 1. (a) IP and OOP magnetization curves of Ta/Pt/[Co/Pt]₄/Co/Ta blanket film at RT. Inset shows the OOP hysteresis loop showing perpendicular anisotropy of the blanket film with coercivity $H_c \approx 300$ Oe. (b) Device schematic depicting current delivery along the x-axis and anomalous Hall voltage V_H measurement along the Hall bar. (c) H_c obtained from $R_H - H_z$ measurements in a scanning OOP magnetic field from room temperature from RT to 360 K show an inverse relationship of coercivity with temperature. Insets show square $R_H - H_z$ loops at RT and 360 K. The change in R_H is $2\ \Omega$ for device temperatures in the measurement range.

and probing currents I , corresponding to a current density J , applied along the channel. Post-fabrication, the magnetization of the device was probed by measuring the anomalous Hall voltage V_H across the Hall bar by applying a non-perturbing DC probing current $I_{\text{probe}} = 200\ \mu\text{A}$. The anomalous Hall resistance R_H , defined as a measure of the degree of perpendicular magnetization in the device, can be determined from $R_H = V_H/I_{\text{probe}}$. R_H is plotted as a function of an out-of-plane (OOP)

magnetic field H_z to show the bipolar magnetization switching of the Hall cross structure. Individual $R_H - H_z$ hysteresis loops for each point in the plot of Fig. 1(c) are shown in Supplementary Material S1. From $R_H - H_z$ measurements at RT up to $T = 360$ K, the coercivity of the device was observed to decrease monotonically with increasing temperature as shown in Fig. 1c. However, the change in Hall resistance ΔR_H generally remains to be $2\ \Omega$ across the range of measured device temperatures. The Hall resistance amplitude and squareness of the hysteresis loops were invariant in the range of measured device temperatures. The inset shows the hysteresis loops obtained at RT and 360 K for comparison.

To study the current-induced magnetization switching (CIMS) due to the SOT, R_H is plotted against pulsed channel current I_{ch} . Each measurement loop begins with an injection of a 1 ms initialization pulse $I_{\text{init}} = -24$ mA to set a reference magnetization state. Subsequently, 1 ms write pulses I_{ch} up to $+24$ mA in steps of 1 mA are delivered. A probing current $I_{\text{probe}} = 200\ \mu\text{A}$ after each write pulse is used to measure R_H . Throughout the measurement sequence, the device is subjected to a static IP field $H_x = 1$ kOe along the direction of current flow to break the switching symmetry required for deterministic SOT switching. Fig. 2a shows the $R_H - I_{\text{ch}}$ loops at various current amplitudes at RT. The devices exhibit multi-state behaviour with R_H dependent on the amplitude of I_{ch} . No further change in R_H was observed beyond $I_{\text{ch}} = I_{\text{sat}} = 24$ mA indicating that SOT-driven magnetization switching has reached saturation. Intermediate values of the device's magnetization state can be achieved by regulating the amplitude of the current pulses up to $+24$ mA. Fig. 2b shows *in-situ* Kerr images of the device magnetization state at current amplitudes of 5 mA, 18 mA, 20 mA, and 23 mA.

The smaller ΔR_H in CIMS can be attributed to the partial magnetization switching at the device junction, as compared to the complete magnetization reversal due to an externally-applied OOP magnetic field. To obtain an accurate current density profile, current flow through the device was modelled in COMSOL (see Supplementary Material S2) and plotted in Fig. 3a. The inhomogeneous current-density is due to lateral shunting of the current at the device junction. Furthermore, the progressive magnetization switching is also observed at the device junction, as evident from the Kerr microscopy images. Subsequently, the progression of magnetization switching in the Hall cross structure was simulated in Mumax3 (see Supplementary Material S3), using the current density profile data derived from COMSOL [24]. The material parameters used in the simulations are $M_s = 7.6 \times 10^5\ \text{A m}^{-1}$, $K_u = 3.8 \times 10^5\ \text{J m}^{-3}$, and $A_{\text{ex}} = 1.5 \times 10^{-11}\ \text{J m}^{-1}$. By mapping the current density J as an effective OOP field $H_{z,\text{eff}}$, similar behaviour in magnetization switching was observed. The snapshots for increasing $H_{z,\text{eff}}$ modelled in the micromagnetic simulation is presented in successive order in Fig. 3b. The domain growth at the junction of the simulated device closely resembles that as observed through *in-situ* Kerr microscopy of the physical device. We compare the Kerr microscopy images of magnetization states between current-induced SOT and OOP field switching methods in Supplementary Material S4. Since the degree of magnetization switching is dependent on the amplitude of $J \propto H_{z,\text{eff}}$, the ratio between $H_{z,\text{eff}}$ and J can effectively be used to quantify the efficiency $H_{z,\text{eff}}/J$ which will be described in the next section.

As the characteristics of magnetic materials and devices are temperature-dependent, it is imperative to understand how thermal effects can affect magnetization switching due to current-induced SOTs. To study the temperature-dependence of ΔR_H due to CIMS, the $R_H - I_{\text{ch}}$ measurement sequence is repeated at varying temperatures up to 360 K. Fig. 4a shows ΔR_H and critical switching current I_{sw} from RT to 360 K in the presence of IP field $H_x = 2.8$ kOe. Here, I_{sw} is defined as the current at which ΔR_H changes by 50%. At room temperature, I_{sw} is 17 mA and drops to 13 mA when the device temperature is increased up to 360 K. While the device shows monotonic decrease in I_{sw} with increasing temperatures, ΔR_H is observed to increase up to 340 K due to weakened anisotropy, lowering the energy barrier between states and resulting in

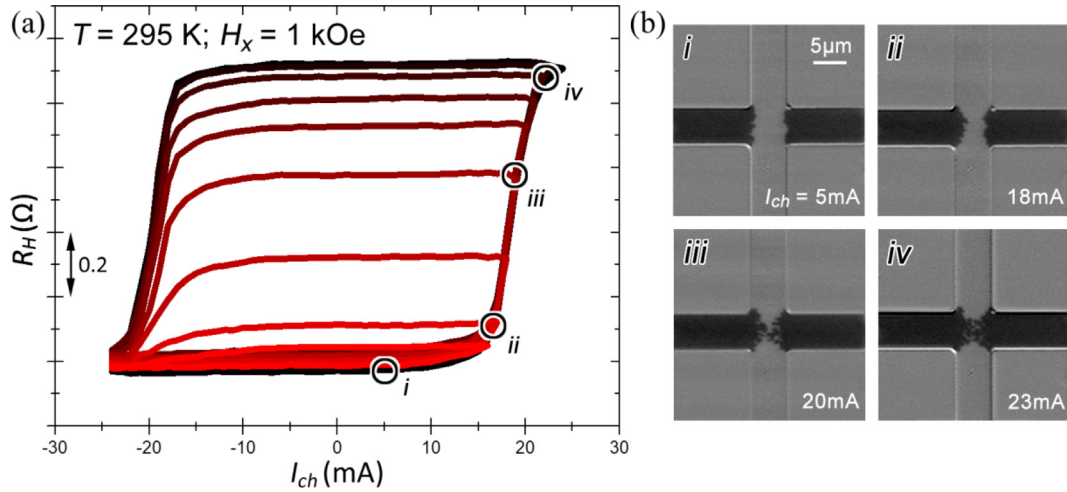


Fig. 2. (a) $R_H - I_{ch}$ loops at RT showing intermediate resistance states, and (b) Kerr microscopy images of device magnetization configuration at various I_{ch} corresponding to the measured Hall resistances.

thermally-assisted current-induced SOT switching. Further increase in temperature beyond 340 K results in a decrease in ΔR_H , revealing that some of the magnetic domains may have substantially weakened anisotropy to the point where much of the perpendicular magnetization is not sustained under the IP field. By varying both H_x and T , a phase diagram describing the switching behaviour of the devices is obtained as shown in Fig. 4b. The polarity of I_{ch} and H_x results in LRS-to-HRS or HRS-to-LRS loops. A large H_x is required for CIMS in highly anisotropic Co/Pt multilayer systems and can be observed in the region of red of the phase diagrams where the largest ΔR_H is achieved. For $H_x < 0.28$ T, ΔR_H generally increases with T . Throughout the T -dependent measurements, $R_H - H_z$ loops were performed to confirm that there were no irreversible changes to the magnetic properties of the device due to the combined effects of thermal and Joule heating.

To quantify the SOT efficiency of the device at room and peak T , the $H_{z,eff}$ due to I_{ch} at RT and 360 K was determined. For this measurement, a calibrated air-core electromagnet was used to provide a sweeping H_z field as shown in the schematic Fig. 5a. The sample was located at the centre of the air-core electromagnet during measurement. The Hall resistance R_H in a scanning OOP field H_z was measured at varying channel currents I_{ch} and IP field H_x . The loop shifts for $I_{ch} = \pm 12$ mA with their loop centres displaced due to opposite current polarities is shown in Fig. 5b. The vertical offsets are for clarity. Fig. 5c shows the depinning fields for down-to-up (blue dots) and up-to-down (red dots) switching transitions across a range of I_{ch} from -12 mA to $+12$ mA. The loop shift (black dots) determined from the depinning fields (zero-crossing) is defined to be the effective field $H_{z,eff}$ at the respective H_x .

The set of loop shifts at $H_x = \pm 10$ mT clearly shows that the loop shift is dependent on the current polarity as shown in Fig. 5d. Here, a linear fit approximates the efficiency χ . This measurement is performed across $H_x = \pm 1$ kOe at RT and 360 K. The χ versus H_x is plotted in Fig. 5e and 5f for RT and 360 K, respectively. At RT, $\chi_{sat}(RT) \approx 74$ Oe/ 10^{11}Am^{-2} , comparable to reported values in single Pt/Co and Pt/CoFeB stacks [25]. At $T = 360$ K, the value of $\chi_{sat}(360 \text{ K}) \approx 59$ Oe/ 10^{11}Am^{-2} . The relationship between χ and the spin Hall angle (SHA) θ_{SH} of the HM layers is given by $\chi_{sat} = \frac{\pi}{2} \frac{6_{SH} \hbar}{2eM_s t_{FM}}$, where \hbar , e , M_s and t_{FM} are the Planck's constant, electron charge, saturation magnetization, and FM layer thickness, respectively [26]. The SHA of Pt θ_{SH}^{Pt} has been reported to be largely invariant with temperature up to 400 K [27–30]. However, the damping-like efficiency of Ta ξ_{DL}^{Ta} has been reported to decrease monotonically with increasing temperature from 300 K [31]. The damping-like efficiency ξ_{DL} , spin Hall angle θ_{SH} , and SOT efficiency χ_{sat} are figures of merit that scale with each other [25,29]. Therefore, the decrease of χ_{sat} by 26% from 295 K and 360 K can be attributed to the corresponding decrease in ξ_{DL}^{Ta} and θ_{SH}^{Pt} at higher device temperatures.

By adopting a current-driven domain wall propagation model [32], the external field sufficient to overcome the effective field due to the Dzyaloshinskii-Moriya interaction (H_{DMI}) can be determined. At both ends of the temperature range, $H_{DMI}(RT) \approx 655$ Oe and $H_{DMI}(360 \text{ K}) \approx 560$ Oe. The decrease in H_{DMI} and weakening of DMI strength with increasing T is due to greater thermal disorder [33,34]. The chiral magnetization canting due to DMI can be overcome with smaller IP bias field H_x at higher temperature T .

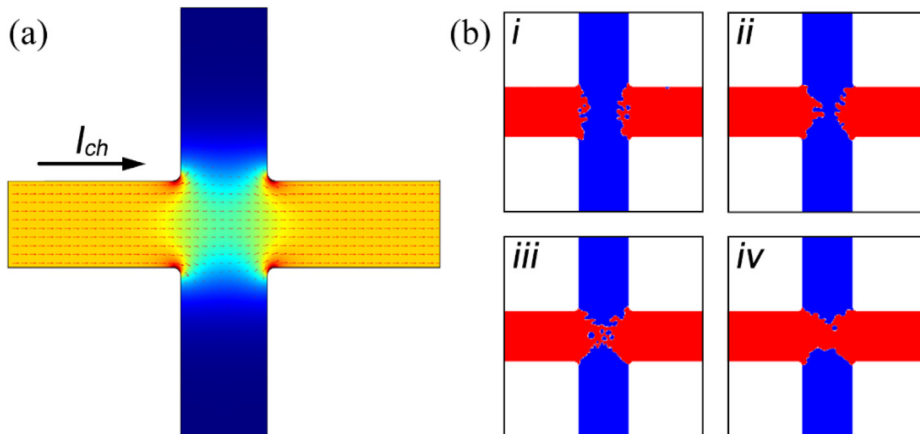


Fig. 3. (a) Current density profile across the device due to current I_{ch} . Lateral shunting of the current at the device junction results in inhomogeneous current-density. (b) Sequential snapshots of up (red) and down (blue) magnetic domains as the amplitudes of current-induced OOP effective fields are increased from (i) to (iv). In this sequence, the down magnetic domains gradually flip up across the device. (For interpretation of the references to colour in this figure legend, the reader is referred to the web version of this article.)

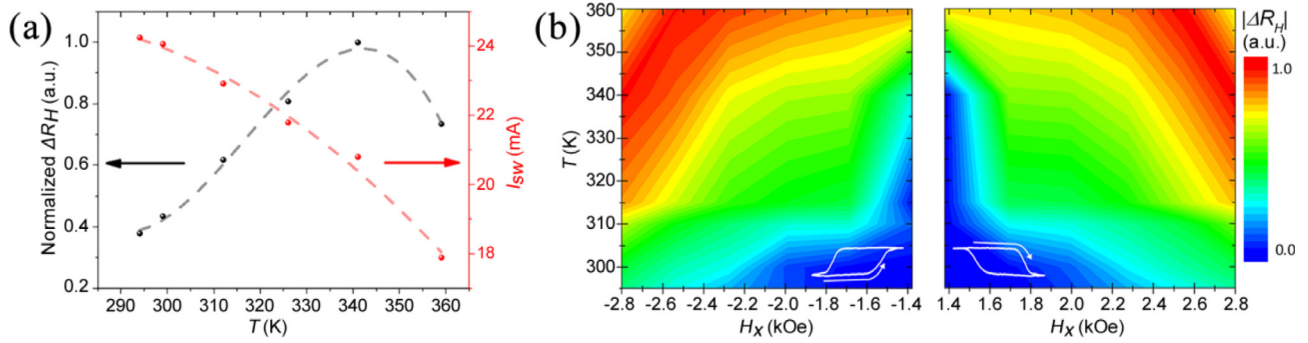


Fig. 4. (a) Thermally-assisted switching at 2.8 kOe results in monotonic decrease in switching current I_{sw} with increasing temperature T . The change in Hall resistance ΔR_H peaks at 340 K as the reduced anisotropy is unable to sustain a fully OOP magnetization above that temperature. (b) Phase diagrams across varying IP fields show ΔR_H due to 1 ms write pulses across varying IP bias field H_x .

Table 1 compares the H_{DMI} values obtained from other works using the same techniques [25,35,36]. The [Co/Pt]₄/Co multilayer in this work suggests that opposing DMI at the interfaces of each Co layer would interfere. Therefore, the H_{DMI} determined from this

measurement method describes only the net effect from the entire multilayer stack.

The intermediate magnetization states are persistent and therefore non-volatile with successive read operations. Bipolar pulse switching

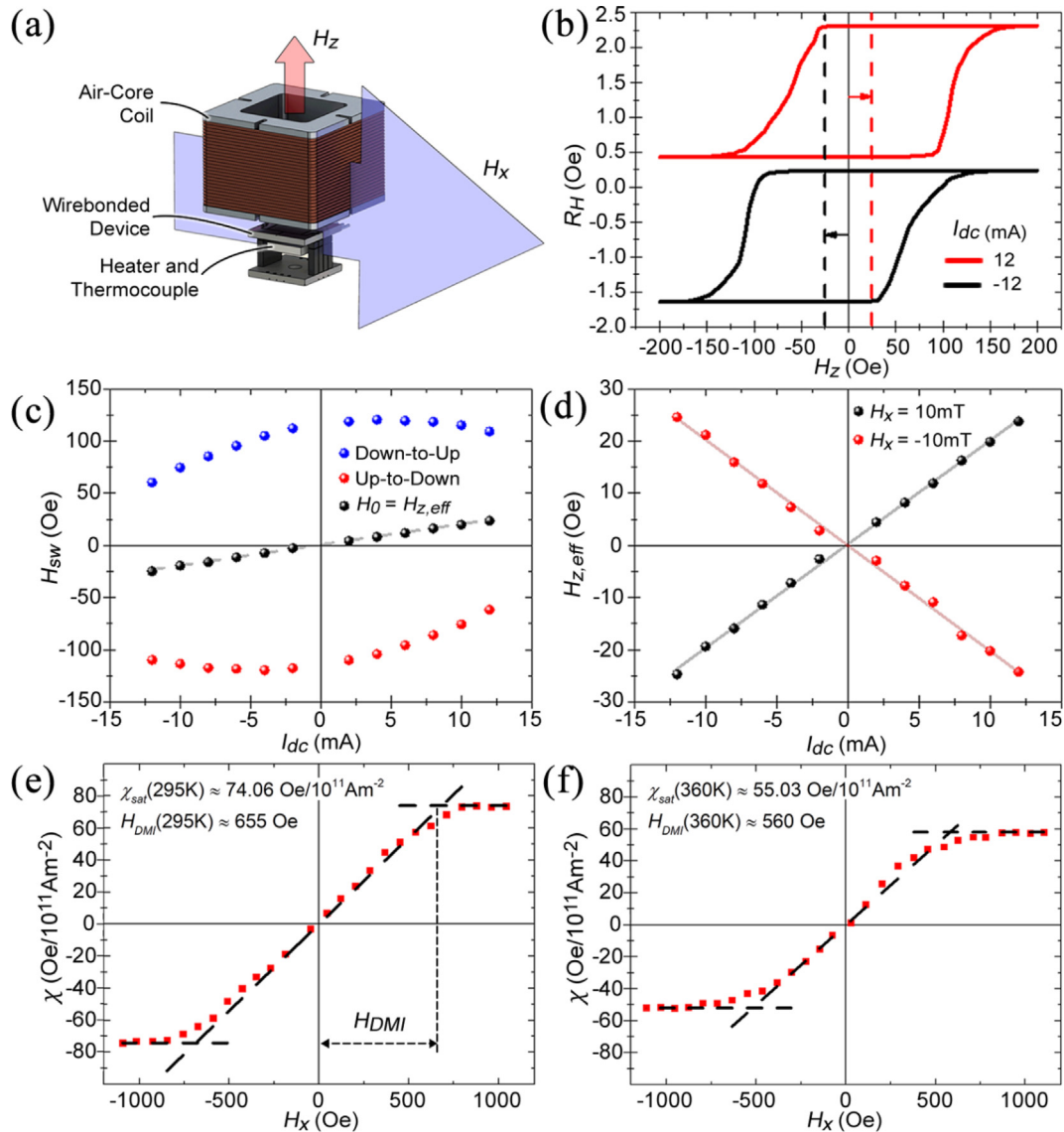


Fig. 5. (a) Schematic of measurement set-up showing heater with integrated thermocouple, and air-core coil providing an OOP magnetic field H_z . A larger electromagnet (not shown) provides an IP H_x field. (b) $R_H - H_z$ loop at RT for $H_x = 0.1$ T and $I_{probe} = \pm 12$ mA showing shifts in loop centers. Vertical offset is for clarity. (c) Loop shift (black dots) due to I_{probe} . (d) Loop shifts due to bias fields of opposite polarity. Effective field χ for (e) $T = RT$ and (f) $T = 360$ K.

Table 1

Comparison table of H_{DMI} values obtained from similar measurement methods. Values of H_{DMI} obtained in this and other works using similar measurement methods of determining χ [25,35,36].

Multilayer Stack	$ H_{DMI} $ (Oe)	Reference
Pt (4)/Co (1.2)/Ir (1)	655	Durga Khadka, et al.
Pt (4)/Co (1.2)/Ir (2)	813	
Pt (4)/Co (1)/Ir (1)	1300	
Pt (4)/Co (1)/Ir (2)	1404	
Pt (4)/Co (0.8)/Ir (2)	2120	
Pt (4)/Co (0.8)/Ir (3)	2180	
Pt (4)/Co (0.8)/Ir (4)	2386	Chi-Feng Pai, et al.
Pt (3)/[Pt (1)/Co (0.8)/Ru (1.3)] ₂	2200	
Pt (4)/Co (1)/MgO (2)	2800	Jiangwei Cao, et al.
Ta (6)/CoFeB (1)/MgO (2)	250	
Ta (3)/CoFeB (1.3)/MgO (1)/Ta (1)	300	
Pt (3)/[Co (0.6)/Pt (0.6)] ₄ /Co (0.6)/Ta (5)	655 (RT = 295 K); 560 (360 K)	This work

followed by successive reads at varying temperatures from RT to 360 K is performed to demonstrate this. At each temperature setpoint, alternating polarities of current pulses are delivered in the presence of an external magnetic field of $H_x = +1$ kOe as shown in Fig. 6a. The write pulses are each followed by successive read operations in the absence of the external magnetic field. ΔR_H for each current amplitude at varying

temperatures is described in the phase diagram as shown in Fig. 6b. At $T = RT$, more intermediate resistance states are accessible, as indicated by the broadening of the colour map at increasing fields. Elevated temperatures result in a reduction of field required for switching to achieve the same resistance state at $T = RT$ as indicated by the eroding dark blue region. Even though switching occurs across the range of temperatures, receding red regions indicate that the degree of magnetization switching deteriorates at elevated temperatures.

The effect of temperature on the reliability of writing and reading a multi-state resistance device may pose a challenge. However, this can be resolved by using a variation sensing circuit to compensate for a change in device temperature, and perform corrected write and read operations accordingly [23,37,38]. On the other hand, the device can serve as a temperature sensor by utilizing its temperature sensitivity. [39] Under certain write currents, different magnetization states can result from different device temperatures. A threshold used to differentiate between temperature ranges and boundaries can be implemented.

2. Conclusion

In summary, SOT-driven multi-state magnetization switching in Co/Pt Hall cross devices were demonstrated for devices operating from RT to 360 K. The multilayer shows strong as-deposited perpendicular magnetic anisotropy. The anomalous Hall resistance scales with current amplitude, and the multi-state characteristic of a current-induced SOT

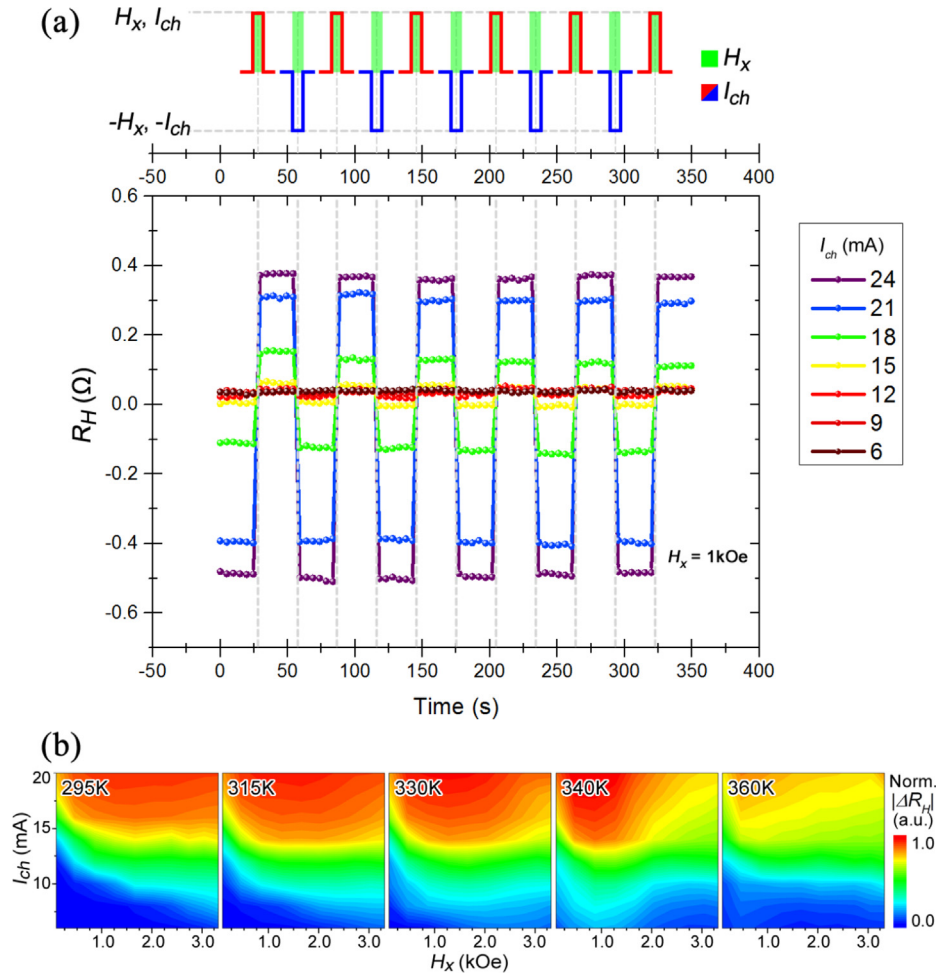


Fig. 6. (a) Procedure for multistate write and read involves applying a write pulse I_{ch} in the presence of an IP field H_x . The resistance state is probed with a non-perturbing $I_{probe} = 200$ μ A. The procedure is repeated with alternating polarities and amplitudes of I_{ch} . (b) Phase diagram for multistate write and read across varying temperatures T and IP bias field H_x .

switched device was shown to be due to a geometrically imparted, inhomogeneous current density distribution across the device junction. The current-induced SOT switching was simulated by mapping the current density profile across the device to an effective OOP field. The simulation results closely mimic the device magnetization states as observed through *in-situ* Kerr microscopy imaging at various pulse current amplitudes. When the device was subjected to the temperature range from RT to 360 K, the switching amplitude derived from the change in Hall resistance first increases up to about 340 K before decreasing. While the switching current I_{sw} is inversely proportional to device temperature, the change in high and low resistance states ΔR_H is greatest at 340 K. The effective OOP field per unit current density χ was quantified at RT ($\chi_{sat}(RT) \approx 74 \text{ Oe}/10^{11} \text{ Am}^{-2}$) and 360 K ($\chi_{sat}(360 \text{ K}) \approx 59 \text{ Oe}/10^{11} \text{ Am}^{-2}$). The efficiency, saturation field, and IP field required to overcome the DMI field are reduced at elevated temperatures due to increase in thermal disorder. This work gives additional insight on the effect of elevated temperature on SOT-driven multi-state devices. The challenges imposed by the temperature sensitivity of multi-state write and read can be resolved with appropriate sensing circuits to monitor and compensate for the temperature variation. Alternatively, the device can serve as a temperature sensor, by exploiting the temperature-dependent current-induced SOT switching.

CRedit authorship contribution statement

G.J. Lim: Conceptualization, Investigation, Methodology, Data curation, Writing - original draft. **W.L. Gan:** Investigation, Writing - review & editing. **W.C. Law:** Investigation, Writing - review & editing. **C. Murapaka:** Writing - review & editing. **W.S. Lew:** Funding acquisition, Project administration, Supervision, Writing - review & editing.

Declaration of Competing Interest

The authors declare that they have no known competing financial interests or personal relationships that could have appeared to influence the work reported in this paper.

Acknowledgements

The work was supported by the Singapore National Research Foundation, under a Competitive Research Programme (Non-volatile Magnetic Logic and Memory Integrated Circuit Devices, NRF-CRP9-2011-01), and an Industry-IHL Partnership Program (NRF2015- IIP001-001). The support from an RIE2020 ASTAR AME IAF-ICP Grant (No. I1801E0030) is also acknowledged.

Appendix A. Supplementary data

Supplementary data to this article can be found online at <https://doi.org/10.1016/j.jmmm.2020.167201>.

References

- [1] M.I. Dyakonov, V.I. Perel, Current-induced spin orientation of electrons in semiconductors, *Phys. Lett. A* 35 (6) (1971) 459–460.
- [2] L. Liu, et al., Current-induced switching of perpendicularly magnetized magnetic layers using spin torque from the spin hall effect, *Phys. Rev. Lett.* 109 (9) (2012) 096602.
- [3] X. Wang, A. Manchon, Diffusive spin dynamics in ferromagnetic thin films with a Rashba interaction, *Phys. Rev. Lett.* 108 (11) (2012) 117201.
- [4] H. Kurebayashi, et al., An antidamping spin-orbit torque originating from the Berry curvature, *Nat. Nanotechnol.* 9 (2014) 211.
- [5] X. Qiu, et al., Spin-orbit-torque engineering via oxygen manipulation, *Nat. Nanotechnol.* 10 (2015) 333.
- [6] E. van der Bijl, R.A. Duine, Current-induced torques in textured Rashba ferromagnets, *Phys. Rev. B* 86 (9) (2012) 094406.
- [7] K.-W. Kim, et al., Magnetization dynamics induced by in-plane currents in ultrathin magnetic nanostructures with Rashba spin-orbit coupling, *Phys. Rev. B* 85 (18) (2012) 180404.
- [8] D.A. Pesin, A.H. MacDonald, Quantum kinetic theory of current-induced torques in Rashba ferromagnets, *Phys. Rev. B* 86 (1) (2012) 014416.
- [9] I.M. Miron, et al., Perpendicular switching of a single ferromagnetic layer induced by in-plane current injection, *Nature* 476 (7359) (2011) 189–193.
- [10] S. Emori, et al., Current-driven dynamics of chiral ferromagnetic domain walls, *Nat. Mater.* 12 (7) (2013) 611–616.
- [11] K.-S. Ryu, et al., Chiral spin torque at magnetic domain walls, *Nat. Nanotechnol.* 8 (2013) 527.
- [12] J. Torrejon, et al., Interface control of the magnetic chirality in CoFeB/MgO heterostructures with heavy-metal underlayers, *Nat. Commun.* 5 (2014) 4655.
- [13] Q.Y. Wong, et al., In situ Kerr and harmonic measurement in determining current-induced effective fields in MgO/CoFeB/Ta, *J. Phys. D Appl. Phys.* 51 (11) (2018) 115004.
- [14] R.H. Liu, W.L. Lim, S. Urazhdin, Dynamical skyrmion state in a spin current nano-oscillator with perpendicular magnetic anisotropy, *Phys. Rev. Lett.* 114 (13) (2015) 137201.
- [15] A.A. Awad, et al., Long-range mutual synchronization of spin Hall nano-oscillators, *Nat. Phys.* 13 (2016) 292.
- [16] A. Kurenkov, et al., Device-size dependence of field-free spin-orbit torque induced magnetization switching in antiferromagnet/ferromagnet structures, *Appl. Phys. Lett.* 110 (9) (2017) 092410.
- [17] A. van den Brink, et al., Field-free magnetization reversal by spin-Hall effect and exchange bias, *Nat. Commun.* 7 (2016) 10854.
- [18] S. Fukami, et al., Magnetization switching by spin-orbit torque in an anti-ferromagnet-ferromagnet bilayer system, *Nat. Mater.* 15 (2016) 535.
- [19] A.B. William, et al., Analogue spin-orbit torque device for artificial-neural-network-based associative memory operation, *Appl. Phys. Express* 10 (1) (2017) 013007.
- [20] J. Grollier, D. Querlioz, M.D. Stiles, Spintronic nanodevices for bioinspired computing, *Proc. IEEE* 104 (10) (2016) 2024–2039.
- [21] T. Andy, Memristor-based neural networks, *J. Phys. D Appl. Phys.* 46 (9) (2013) 093001.
- [22] W. Kang, et al., Reconfigurable codesign of STT-MRAM under process variations in deeply scaled technology, *IEEE Trans. Electron Devices* 62 (6) (2015) 1769–1777.
- [23] B. Wu, et al., Temperature impact analysis and access reliability enhancement for 1T1MTJ STT-RAM, *IEEE Trans. Reliab.* 65 (4) (2016) 1755–1768.
- [24] A. Vansteenkiste, et al., The design and verification of MuMax3, *AIP Adv.* 4 (10) (2014) 107133.
- [25] C.-F. Pai, et al., Determination of spin torque efficiencies in heterostructures with perpendicular magnetic anisotropy, *Phys. Rev. B* 93 (14) (2016) 144409.
- [26] J. Han, et al., Room-temperature spin-orbit torque switching induced by a topological insulator, *Phys. Rev. Lett.* 119 (7) (2017) 077702.
- [27] Y. Wang, et al., Determination of intrinsic spin Hall angle in Pt, *Appl. Phys. Lett.* 105 (15) (2014) 152412.
- [28] K. Nakagawara, et al., Temperature-dependent spin hall effect tunneling spectroscopy in platinum, *Appl. Phys. Lett.* 115 (16) (2019) 162403.
- [29] C.-F. Pai, et al., Dependence of the efficiency of spin Hall torque on the transparency of Pt/ferromagnetic layer interfaces, *Phys. Rev. B* 92 (6) (2015) 064426.
- [30] P. Phu, et al., Bolometric ferromagnetic resonance techniques for characterising spin-Hall effect at high temperatures, *J. Magn. Mater.* 485 (2019) 304–307.
- [31] J. Kim, et al., Anomalous temperature dependence of current-induced torques in CoFeB/MgO heterostructures with Ta-based underlayers, *Phys. Rev. B* 89 (17) (2014) 174424.
- [32] T.Y. Tsai, et al., Spin-orbit torque magnetometry by wide-field magneto-optical Kerr effect, *Sci. Rep.* 8 (1) (2018) 5613.
- [33] S. Schlotter, P. Agrawal, G.S.D. Beach, Temperature dependence of the Dzyaloshinskii-Moriya interaction in Pt/Co/Cu thin film heterostructures, *Appl. Phys. Lett.* 113 (9) (2018) 092402.
- [34] Y. Zhou, et al., Temperature dependence of the Dzyaloshinskii-Moriya interaction in ultrathin films, *Phys. Rev. B* 101 (5) (2020) 054433.
- [35] D. Khadka, S. Karayev, S.X. Huang, Dzyaloshinskii-Moriya interaction in Pt/Co/Ir and Pt/Co/Ru multilayer films, *J. Appl. Phys.* 123 (12) (2018) 123905.
- [36] J. Cao, et al., Spin orbit torques induced magnetization reversal through asymmetric domain wall propagation in Ta/CoFeB/MgO structures, *Sci. Rep.* 8 (1) (2018) 1355.
- [37] S.Z. Rahaman, et al., Pulse-width and temperature effect on the switching behavior of an Etch-Stop-on-MgO-barrier spin-orbit torque MRAM cell, *IEEE Electron Device Lett.* 39 (9) (2018) 1306–1309.
- [38] S. Wang, et al., MTJ variation monitor-assisted adaptive MRAM write, 2016 53rd ACM/EDAC/IEEE Design Automation Conference (DAC), (2016).
- [39] A. Sengupta, et al., Magnetic tunnel junction as an on-chip temperature sensor, *Sci. Rep.* 7 (1) (2017) 11764.